Fig. 13   Results for reader 1 for image quality 1 (normal 10 cases and abnormal 10 cases)
Explanation of operating points for the (1),(2),(3) the same as for Fig. 11
and Az as the function of of the image quality for this method and the 4-step confidence score
method

Fig. 12 shows the ROC curves drawn on the basis of determining the estimated confidence level p for each of readers 2 through 8 for image quality levels 1-5, using the same method as that for reader 1. Excluding reader 8, the estimated ROC curves for readers 1-7 are drawn with interpolation between the operating points by the near-normal method as for reader 1.

Fig. 13 shows the estimated ROC curves and the Az values at each of the image quality levels (10 normal and 10 abnormal cases) for reader 1. While the number of films examined has decreased to 1/5 the number in Fig. 11, this figure suggests that estimated ROC curves of operating points composed of continuous confidence level are obtained. The Az values for image quality levels 1, 2, and 3 were approximately comparable, but those for image quality levels 4 and 5 were sharply lower. It can also be seen that the horizontal axis for the operating points for judgments of 0 and 1 was higher.

6. DISCUSSION

As shown in Fig. 1, a person forced to choose between two options is trapped in a state of psychological conflict, a phenomenon that has been understood since ancient times. It is also known that the degree of this conflict is manifested as a prolongation of the judgment time[1-6]. However, there are few research reports observing that this phenomenon

occurs in the setting of image diagnosis. The authors observed this phenomenon in an observer performance study conducted to analyze the line of gaze of dentists[8]. The basic outline for the DDC model was announced at CARS2000 [7], but the reliability of the model had not been thoroughly evaluated at this time. Subsequently, similar tendencies were observed in an observer performance study using other medical images conducted by our group[9,10,11], and in an observer performance study conducted by other authors[12], providing the assurance that this phenomenon is universal. Therefore, in the present report, we first endeavored to restructure the deterministic model (DDC model) to explain the relationship between confidence level and judgment time. Next, based upon the t-p curve derived from this DDC model, we estimated the continuous confidence levels p that are independent of reader introspection from actual observed t values, and proposed a method for drawing ROC curves, even for dichotomous reader judgments of 0 and 1.

The need to draw ROC curves from judgments of 0 and 1 arises from the findings presented below. In brief, even when readers are instructed to use a 4 or 5-step score or continuous confidence level for ROC analysis of diagnostic performance, there are some who will not (or cannot) follow this instruction, that even when the instructions are followed at the commencement of reading, a tendency is gradually seen for 0 and 1 judgments to occur as the reading task progresses, and that tendency is especially reinforced when there is a large number of images to be read[13].

In the following, we discuss the characteristics of the DDC model proposed in this report and the problems and significance of its application for generating ROC curves from the results of 0 and 1 judgments, based on the results of the observer performance study conducted in the present research.

The factors affecting the results of image diagnosis would appear to be numerous, but those first introduced in the present model are k and c. These are parameters relating to the overall process from the commencement of the reader's judgment t=0 until a confidence level p* between 0 and 1 is reached, during conflict between normal (n) and abnormal (p), requiring a certain judgment time t. The parameter k is an integral coefficient that is common to all the images to be read, including such factors as the image quality and the reader's skill, and is a proportionality factor for enlarging or shrinking the overall t-p curve shown in Fig. 5. The parameter c is known as the induction coefficient (Equation (1)), which represents the ease (or difficulty) of making different diagnoses for each image to be read. When the relationship between c and p* for the cases for which images were interpreted in the present research is compared to the simulation in Fig. 2, there were many cases with c>0. The fact shows that it becomes easier to diagnose an abnormal case as abnormal, and at that time, the judgment time shown in Fig. 5 becomes shorter. In contrast, the fact that there were few cases with c<0 shows that there were scant situations in which it was easy to diagnose a normal case as normal, and it can be inferred that the judgment time in such a scenario will increase. That the judgment time for abnormal cases is shorter than that for normal cases in the table in Fig. 10 (3) appears to be a result that reflects this parameter c.

The finding in this report that deserves the most emphasis is the difference between the p-t curve obtained from p(t) (Fig. 4) represented by Equation (6) and the t-p curve according to t(p) (Fig. 5) represented by Equation (4). In short, while p(t) describes the p-t curve from t=0 to t=∞, t(p) signifies the t-p curve until h-fold $(0 \leq h < 1)$ the confidence level p* attained over an unlimited time by the reader, the time he discontinues his thoughts. Both are theoretical estimates derived from the DDC model but it is possible that the latter (t-p curve) represents the relationship between the actual confidence level and the judgment time. As well, this t-p curve is similar in shape to the actual values in Fig. 8, and it may correspond with observed values. In contrast, p(t) shows a process of gradual equilibration of the reader's state of conflict with t, but it is not possible to observe this state.

Next, Equations (4) and (6) of the DDC model warrant attention because they assume that the judgment commences with supposition S assumed immediately before interpretation (time t=0). S is interchangeable with preconception or bias. In brief, as shown in Fig. 6, S can be selected arbitrarily from 0 to 1. When a dichotomous judgment of normal or abnormal commences from S=0 (in other words, p(0)=0), the image diagnosis is assumed to have commenced on the supposition that p=0 (normal) for the reader beforehand. Reading in such a scenario is applicable to image interpretation in lung cancer screening, which seeks to detect lung cancer in 1 of 1000 individuals. In contrast, commencing judgment of normal or abnormal from S=1, or in other words, p(0)=1, indicates that the reader has commenced reading on the prior supposition of abnormal. In such a scenario, suspicion of lung cancer is identified on lung cancer screening, and image diagnosis is carried out when further evaluation is obtained at a specialist hospital. However, either commencing the reading process from S=0 or S=1, the t-p curves derived from Equation (4) are, as seen in Fig. 6, show a high confidence level of >0.5 is reached in a short time for cases in which abnormality is strongly suspected (c>>0) or a low confidence

168

level of <0.5 is reached for cases which are clearly thought to be normal (c<<0). The closer one approaches c=0, the longer the judgment time because of the increased conflict between normal and abnormal, and the final confidence level is determined in the vicinity of 0.5. As a result, the t-p relationship for the overall images is, as shown in Fig. 6, (if the easy-to-diagnose and difficult-to-diagnose cases are even distributed in the sample), a bell-shaped relationship for both S=0 and S=1. Observed values similar to those situations are shown in Fig. 8 (for readers 1-7). (However, that is not the case for reader 8. The cause was possibly that the collection of line of gaze data from the eye camera was incomplete. Because of theoretical limitations on the apparatus and the eye characteristics of the subjects, it appears that the line of gaze data could not be collected with high precision for a certain percentage of subjects[8]. At that time, the observed judgment time (image searching time) becomes inaccurate. Because it is possible that such a scenario is applicable in this case, we continue this discussion below with the results for reader 8 excluded.

This DDC model is first, premised on the assumption that the reader's judgment time t is accurate. Consequently, a further fundamental premise assumes that the t-p curve derived from Equation (4) has the bell-shaped t-p relationship shown in Fig. 5 for reading results for each image quality in the image database for each reader. As a result of this, the confidence level p imagined unconsciously in the mind of the reader is estimated from the observed values t, as shown in Fig. 9. Fig. 11 (1) is the ROC curve drawn on the basis of the p value estimated from the actual measured judgment time t for 50 normal and 50 abnormal cases at image quality levels 1-5 for reader 1. The estimated ROC curve is drawn so that the operating points are interpolated when the responses are made in a 4-step scoring scale. The operating points of the estimated ROC curve are composed of many pairs of (cumulative number of FPs and cumulative number of TPs) obtained from 50 normal and 50 abnormal individuals for whom images are read. Hence, it can be anticipated that the area under the ROC curve (Az) will be calculated with higher precision than by the usual method (4-step score). As well, Fig. 11 (2) suggests that similar ROC curves will be obtained, even when the scenario involves 0 and 1 judgment. Furthermore, the result in Figure 12 indicates that the situation was the same for the other readers (2-7). (Provided, however, that reader 8 is excluded for the reasons provided above (possible inaccuracy in the measurement of judgment time).) The result in Fig. 13 shows that even with a small number of cases, an ROC curve can be obtained that is composed of several pairs of operating points from 10 normal and 10 abnormal cases in the image database.

As shown in Fig. 8 and Fig.10 (2), the judgment time when each reader responded with a confidence level according to the 4-step score scale exhibited a bell shape for t-p overall, but the variation in judgment times at each confidence score was large. It is inferred that the continuous confidence of periphery is a result rounded up into a each score. As shown in Figs. 11-13, the fact that ROC curve based on estimated confidence level p has operating points interpolated between the ROC curves of 4-step scores, supports this.

The above discussion was based on the results of subjecting to ROC analysis, the bell-shaped ROC curves for conditions time t=0, and S=0 or S=1. However, according to this proposed DDC model, as shown in Fig. 6, it is possible to estimate p-t curves and t-p curves for S=0 or S≠1. Intuitively, for example, if the judgment commences from confidence level p=0.5 at time t=0, a judgment that is free of preconceptions can be obtained. However, the judgment time t decreases when p is in the vicinity of 0.5 at time t=0. Similar to the situation for other values of S too, the judgment time decreases in the vicinity of S. On the basis of these results, a general rule for medical judgment can be deduced: "No judgment is free of supposition". However, data for the scenario in which the judgment commences from the supposition S=0 or S≠1 are yet to be observed. In the future, an observer performance study will be required to confirm whether or not these lessons derived from the DDC model are indeed true. As well, there are probably many occasions in actual image diagnosis where the judgment must be made among 3 or more choices. Further investigation of the DDC model to address those scenarios will be necessary.

7. CONCLUSION

We have proposed a diagnosis-dynamic characteristic model (DDC model) to explain the relationship between the reader's judgment time (t) and confidence level (p) when making a dichotomous judgment. Furthermore, by applying the t-p relationship derived from this model, we have presented a method for estimating the reader's psychological probability (confidence rating) from the observed judgment time t. Thus, we have shown that if the judgment time can be measured accurately, the reader's continuous confidence level can be quantified without introspection, and that more

accurate ROC analysis is possible in a scenario in which the response involves the usual 4 or 5-step confidence score, as well as for a dichotomous 0 and 1 judgment too.

ACKNOWLEDGMENTS

REFERENCES

1.D.Cartwrite, Decision-time in relation to the differentiation of the phenomenal field. *Psychol.Rev.,,*48:1941;425-442

2. H.L. Hollingworth, The definition of judgment. *Psychol. Rev.,*32:1925;337-361.

3. P.L. Weber, Judgment tody. . *Psycol. Rev.,*44:1937; 264-266

4. D.M.Johnson, Confidence and speed in two-category judgment. *Arch. Psychol.,* 1939:No.241

5. D.Cartwrite, Relation of decision-time to the categories of response. *Amer. J. Psychol.,*54:1941;220-228

6.J.P.Guilford, Psychometric method. *McGraw-Hill Book Conpany Inc.* New York,1954

7.T.Matsumoto, A.Furukawa, K.Suwa et al., Proposition of the diagnosis-dynamic characteristic model describing the relation between search time and confidence scores on image perception and performance. *Proceedings of CARS2000, Excerpta Medica International Congress Series*1214: 2000; 1051

8. K.Suwa, A.Furukawa, T.Matsumoto et al., Analyzing the eye movement of dentists during their reading of CT images. *Odontology,*89:2001;54-61

9.T.Matsumoto, N.Fukuda, M.Tsutikawa et al., Observer performance study for CT-image reading of one slice or multi-slice by the cine display mode of CRT system- An application of the diagnosis-Dynamic Characteristic (DDC) model. *Proceedings of CARS2001, Excerpta Medica International Congress Series*1230: 2001; 1190

10. T. Matsumoto, N. Fukuda, N. Honda et al,. ROC curve can be generated from a dichotomous judgment without observer-reported scores of diagnostic confidence levels. *SNM2004.6,* Philadelphia

11. T.Matsumoto, A.furukawa, M.Tsutikawa et al., Relationship between changes in pupil size over time and diagnostic accuracy. *Proceedings of SPIE2003,* vol.5034:2003;393-402

12.K.Hidaka, Y.Okura, T.Johkoh et al., Time study of computer aided diagnosis - A preliminary results on temporal Subtraction. *Proceedings of CARS2001, Excerpta Medica International Congress Series*1230: 2000; 565-569

13. T. Matsumoto, M. Matsumoto, Keiichi Nagao et al., An assessment of the potentiality of CT image reporting by medical technologist. *Proceedings of SPIE2005,* vol.5749:2005; 590-600

*matsu@nirs.go.jp; phone 81 43 206-3177; fax 81 43 206-3246

ELSEVIER

MEDICINE

Comparison of bronchoscopic diagnosis for peripheral pulmonary nodule under fluoroscopic guidance with CT guidance

Kenji Tsushima[a,*], Shusuke Sone[a], Takaomi Hanaoka[a], Fumiyoshi Takayama[a], Takayuki Honda[b], Keishi Kubo[c]

[a]Azumi General Hospital, 3207-1 Ikeda-machi, Kitaazumi-gun 399-8695, Japan
[b]Department of Clinical Laboratory, Shinshu University School of Medicine, 3-1-1 Asahi, Matsumoto 390-8621, Japan
[c]First Department of Internal Medicine, Shinshu University School of Medicine, 3-1-1 Asahi, Matsumoto 390-8621, Japan

Summary
Background: A new diagnostic procedure has been established for the selection of appropriate therapy for small lung lesions. We compared the sensitivity of real-time multi-slice computed tomography (MSCT) and X-ray television (TV) fluoroscopic guidance for performing bronchoscopy.
Methods: The first author performed and interpreted all bronchoscopies described in this study. The diagnosis of malignancy or benign was based on the results of histopathological examination, as well as clinical and imaging follow-up MSCT. We also compared the diagnostic yields of lesion size between MSCT and X-ray TV fluoroscopic guidance.
Results: Real-time MSCT and X-ray TV fluoroscopic guidance was conducted in 82 and 78 patients, respectively. The lesion size detected by real-time MSCT and X-ray TV fluoroscopic guidance was <10 mm ($n = 21$, 14), 11–15 mm ($n = 24$, 12), 16–20 mm ($n = 19,14$), 21–25 mm ($n = 9$, 12) and >26 mm ($n = 9$, 26). The sensitivity of real-time MSCT- and X-ray TV fluoroscopic guidance was 62.2% and 52.6%, respectively. The sensitivity of real-time MSCT fluoroscopic guidance for histopathologic diagnosis of lesions less than 15 mm was higher than that of X-ray TV fluoroscopic guidance. While it was difficult to histopathologically diagnose small lung lesions less than 10 mm in diameter, real-time MSCT fluoroscopic guidance offers a better chance of such diagnosis, irrespective of the size of the lesion, compared with X-ray TV fluoroscopic guidance.

*Corresponding author. Tel.: +81 263 37 2631; fax: +81 263 36 3722.
E-mail address: tsushima@hsp.md.shinshu-u.ac.jp (K. Tsushima).
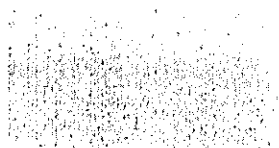
Conclusion: Real-time MSCT fluoroscopic guidance allows the bronchoscopist to accurately determine the location of the instruments in relation to the lesion in real time, thus helping to reduce the number of negative cases.

Introduction

Lung cancer is the primary cause of cancer death. The cure rates have remained low because of the difficulty in detecting early stage disease. Mountain[1] reported that stage IA cancer represented 13% of the total population and that the 5-year survival rate of patients with such tumors was 61%. Surgical treatment is expected to be associated with a fairly high 5-year survival rate for small lung lesions<20 mm without nodal involvement, or even a higher rate for those measuring <15 mm that are often free of nodal involvement.[2,3] Accordingly, a diagnostic technique that can detect cancers at an early stage is needed to reduce the cancer-related mortality.

Bronchoscopy is a minimally invasive alternative to surgical procedures for the diagnosis of peripheral lung nodules. Previous studies on solitary pulmonary nodules have consistently shown that lesion size influences the diagnostic accuracy of bronchoscopy.[4-6] In particular, the yield of bronchoscopy is low in lesions measuring <20 mm located in the outer third of the lung.[7] Thus, other diagnostic procedures or alternative protocols for the diagnosis of small nodules including lung cancers may be preferable in this situation. Of these, CT-guided transthoracic needle biopsy could be considered as a first diagnostic step, especially in very small, peripheral, and easily accessible lesions. However, the techniques carry a high risk of complications, e.g., pneumothorax, and may also be difficult to conduct depending on the exact location of the lesion. Since bronchoscopy is a safe procedure with a low complication rate and allows the examination of the central airways before operation, it is the first diagnostic step in our hospital. In this regard, television (TV) fluoroscopy is limited by the two-dimensional display format that produces the overlap of structures, potentially hindering biopsy of the lung peripheral nodules. On the other hand, the CT scan has been proposed as a useful guidance method to provide a cross-sectional view of the relevant anatomy during the bronchoscopy procedure.[8] Real-time multi-slice CT (rMSCT) fluoroscopy permits real time and precise localization of the bronchoscope tip and needle.[9]

In the present study, we report our experience using rMSCT-guided bronchoscopy, which provides images in real time, and the usefulness and diagnostic accuracy of this procedure for peripheral nodules. We also compared the diagnostic yields of rMSCT fluoroscopic guidance and X-ray TV fluoroscopic guidance for performing bronchoscopy. Specifically, our study was designed to evaluate whether this bronchoscopic procedure offers a possible approach in selected patients.

Materials and methods

Bronchoscopist and pathologist

The first author (K.T.) is a pulmonologist with an extensive 10-year experience in bronchoscopy. In this study, K.T. performed and interpreted all bronchoscopies described in this study, including those on patients of Iiyama Red Cross Hospital. On the other hand, the histopathological diagnosis was conducted by the same pathologist (T.H.) at Iiyama Red Cross Hospital and Azumi General Hospital.

Subjects

Chest CT was performed as a part of a CT screening program. Subjects were all patients with well-defined pulmonary nodules identified by chest CT at the Azumi General Hospital, who required final diagnosis by bronchoscopy to select treatments: surgery and administration of antibiotics, which were performed between November 2001 and January 2003. Informed consent was obtained from each patient prior to the bronchoscopy procedure. To compare the diagnostic yields of rMSCT and X-ray TV fluoroscopic guidance for performing bronchoscopy, we also included patients with peripheral pulmonary nodules, as identified by chest CT at the Iiyama Red Cross Hospital, who underwent bronchoscopy to select treatments between September 1999 and September 2001.

Evaluation prior to bronchoscopy

All patients underwent chest radiography and thin-section high-resolution CT images before rMSCT and X-ray TV fluoroscopic guidance for performing bronchoscopy. The CT images were obtained with

a CT fluoroscope (Toshiba Asteion; Tokyo, Japan) with a scan rotation time of 0.75 s, using continuous 1-mm collimation slices. The location of the nodule was determined on the chest CT. The size and presence of bronchus signs of the lesion were determined from the findings of chest CT. The largest dimensions of the lesion parallel and perpendicular to the bronchus were measured. The largest perpendicular dimension was used to define the size of the nodule when calculating the effect of size on the diagnostic yield.

Construction of virtual bronchoscopy

Three-dimensional endoluminal tracheobronchial simulations can be constructed from thin-section high-resolution CT scans, which reproduce the appearances of major endobronchial abnormalities, as confirmed during bronchoscopy. Virtual broncho-scopy was constructed using in software (Navigator; GE Medical Systems, surface rendering method) based on MSCT images. After the construction of virtual bronchoscopy for each patient, we imaged the actual endobronchial findings using virtual bronchoscopy. We selected the nearest bronchus to the peripheral nodules before performing bronchoscopy.

rMSCT fluoroscopy

The rMSCT fluoroscopy (10 mA, 120 kV, 2-mm section thickness, 0.75 s of rotation) was performed with real-time visualization to help confirm the location of the transbronchial brush, needle aspiration and biopsy forceps. For all patients, the use of a 10 mA technique was sufficient to achieve good image quality and to perform bronchoscopy. The patient was placed head first into the scanner, with the bronchoscopist to the head of the MSCT table. The bronchoscope monitor was placed on the same side of the lung lesion. The radiologist operating the MSCT fluoroscopy in the same room stood on the opposite side of the rMSCT fluoroscope monitor. The rMSCT fluoroscope monitor was positioned on the same side as the bronchoscope monitor, such that it was visible to both the bronchoscopist and radiologist. A button on the control panel permitted the release of the MSCT table, so that the position of the table could be adjusted by the radiologists hand in a sliding mode. All physicians who remained in the room during rMSCT fluoro-scopic imaging wore lead aprons. The bronchoscopist wore an irradiation monitor on the front of the chest to measure the radiation exposure. Another radiologist operating the rMSCT outside of the rMSCT room could replay the image sequence. An rMSCT fluoroscopic image was obtained to correlate the location of the tip within the target lesions. The brush, aspiration needle or biopsy forceps were inserted through the bronchoscope and implanted in the bronchial wall. The site of implantation was imaged with rMSCT fluoroscopy to ascertain whether the tip was directed properly toward the site of the peripheral lesions. Adjustments were made using rMSCT fluoroscopic images to insure an accurate direction, and the instrument was advanced into the lesion. The biopsy forceps, aspiration needle or brush were directed into the lung segment. Further selection of the appropriate subsegmental region was facilitated with rMSCT fluoroscopic sequences. The location of each instrument, the number of instruments pass and the length of time from the start to end of rMSCT scanning and the amount of overall radiation exposure against patients and bronchoscopist were documented. A final rMSCT fluoroscopic image was obtained to document any complications.

X-ray TV fluoroscopic guidance was performed by bronchoscopy using the above methods under X-ray fluoroscopy, and decided the exact position of the biopsy instrument by changing the patient's body position under X-ray fluoroscopy.

Bronchoscopy procedure

After administration of 1 mg atropine sulfate, 100 μg pethidine hydrochloride and airway anesthesia with 4% lidocaine hydrochloride applied orally, patients lay on the table of the MSCT scanner. Arterial oxygen saturation (SpO_2) and heart rate were continuously measured during bronchoscopy by pulse oximetry. Oxygen was administered via a nasal cannula and the flow was adjusted upward from 1 L/min to maintain SpO_2 above 90%.

A variety of flexible fiberoptic bronchoscopes (Olympus, Tokyo); model BF 3C40 (outer diameter; 3.3 mm, forceps channel; 1.2 mm), and BF P10 (outer diameter; 5.0 mm, forceps channel; 2.0 mm) along with their accessories [brushes (BC-201-c-1006, Olympus), aspiration needles (needle; MAJ-65, sheath; NA-1c-1, Olympus) and biopsy forceps (FB-560-1, Olympus)] were used at Azumi general Hospital and Iiyama Red Cross Hospital. All procedures were performed via the transnasal or transoral route under local anesthesia. After visualization of the vocal cords, additional topical anesthetics were applied as needed. All segments of the bronchial tree were visualized. The presence or absence of endobronchial abnormalities was recorded. The bronchoscope was then advanced

to the lobe and segment known to be the location of the lesion. At first, biopsy forceps using BF 3C40 were advanced into the bronchus under broncho-scope guidance to accurately determine the location of the lesion and performed to obtain at least 2 tissue samples. Next, biopsy using BF P10 was performed to obtain larger 2 tissue samples. After the biopsy forceps, the aspiration needle and brushing were advanced into the lesion, the brushing and aspiration needles were then with-drawn. Specimens obtained by biopsy were placed on glass slides and fixed with 10% formalin. If bacterial or fungal infection was suspected, the brush material was smeared on slides, airdried and processed for Giemsa, acid-fast and PAS staining and was cultured.

Histopathological analysis

Certified cytological technologists blinded to the bronchoscopic findings first confirmed that an adequate sample was collected and then conducted cytological analysis. The diagnosis of malignant disease was based on the results of histopathologi-cal analysis of specimens by pathologists also blinded to the bronchoscopic findings. A diagnosis of benign disease was based on results of histo-pathologic examination, as well as clinical and imaging follow-up MSCTs. Surgical pathological diagnosis was compared with the bronchoscope diagnosis in patients who underwent subsequent resections.

Outcome

We divided the final diagnosis into three groups: Incompletion, Negative and Positive. Incompletion as a final diagnosis was the case in which rMSCT fluoroscopic guidance for performing bronchoscopy could not apparently reach the nodules. Negatives were cases in which the surgical diagnosis differed

from the bronchoscopy diagnosis although the biopsy forceps, aspiration needle or brush instru-ments could apparently reach the nodule(s) under rMSCT. Positives were cases in which the surgical diagnosis was similar to that established using bronchoscopy, or histopathological diagnosis by bronchoscopy that showed granuloma or an inflam-matory change, and these findings decreased or disappeared on follow-up CTs.

Statistical analysis

All values described in the text and tables are the group mean $\pm$ standard deviation. One-way analysis of variance, Student's unpaired t-test and Fisher's exact probability test for independence were used for comparisons between the groups. A P-value less than 0.05 was considered statistically significant.

Results

Eighty-two patients were enrolled in the rMSCT fluoroscopic guidance for performing the broncho-scopy arm of this study (Table 1). The patient population consisted of 43 males and 39 females with a mean age of 65.9 ± 12.3 years (range, 20–95 years), and 24 were current or ex-smokers. Of the 82 procedures in which rMSCT fluoroscopy was used along with bronchoscopy, 82 were directed toward abnormalities in the peripheral lung fields. Table 2 shows the final diagnosis based on bronchoscopy, operation, clinical follow-up or follow-up MSCTs. The final diagnosis was established using broncho-scope samples in 51 patients (62.2%). Histological diagnosis showed 27 adenocarcinoma, 1 small cell carcinoma, 1 large cell carcinoma, 3 atypical adenomatous hyperplasia, and 1 lymphoangioma. In 31 patients, bronchoscopy could not assist in establishing the diagnosis. Thirty-two positive

Table 1. Lesion characteristics.

Lesion size (mm)	rMSCT fluoroscopic guidance	X-ray-TV fluoroscopic guidance
< 10	21 (1) [3]	14 (1) [4]
11–15	24 (5) [4]	12 (4) [6]
16–20	19 (8) [12]	14 (6) [11]
21–25	9 (4) [2]	12 (8) [12]
> 25	9 (6) [7]	26 (20) [26]
Total	82 (24) [28]	78 (39) [59]

Data in parentheses are nodules with a positive bronchial sign.
Numbers in square brackets represent cases visible under X-ray fluoroscopy.
rMSCT: real-time multi-slice computed-tomography; TV: television; BF: bronchoscopy.

Table 2   Final clinical diagnosis of patients under rMSCT fluoroscopic guidance.

	Bronchoscopy	Operation	Follow-up CTs	Therapy
Lung cancer	29	21	2	1
AAH	3	0	0	0
Benign tumor	6	1	0	0
Inflammation	13	0	6	0
Total	51	22	8	1

rMSCT: real-time multislice computed tomography; CT: computed tomography; AAH: adenomatous atypical hyperplasia.

Table 3   Final bronchoscopic results of peripheral lesions under rMSCT fluoroscopic guidance.

Lesion size (mm)	Positive	Incompletion	Negative
<10	9 (1) [2]	10 [1]	2
11–15	13 (5) [3]	6 [1]	5
16–20	12 (4) [8]	5 (2) [2]	2 (2) [2]
21–25	8 (4) [1]	0	1 [1]
>25	9 (6) [7]	0	0
Total	51 (20) [21]	21 (2) [4]	10 (2) [3]

rMSCT: real-time multislice computed tomography; data in parentheses are nodules with a positive bronchial sign.
Numbers in square brackets represent cases visible under X-ray fluoroscopy.

cases were diagnosed as malignancy and 19 were diagnosed as benign. In 8 of these 31 patients, diagnosis was established by subsequent CTs. The remaining 22 patients underwent lung lobectomy or video-assisted thoracic surgery. One patient was treated with chemotherapy after diagnosis of a post-operative recurrent lung cancer (Table 2). Nine of 10 negative cases were diagnosed as adenocarcinoma and one was a fibrotic change by surgery. The diagnostic yields that was considered suspicious for malignancy and benign lesions by radiologists based on the chest CT findings were 59.3% (32 of 54) and 64.3% (18 of 28), respectively. The diagnostic yield of bronchoscopy correlated significantly with the lesion size ($P<0.05$).

The mean diameter of 82 peripheral lung lesions was 16.7 mm (range: 5–51 mm). Twenty-eight of 82 (34.1%) lesions could be detected by X-ray TV-fluoroscopy. A bronchus transiting the lesion (bronchus sign) was detected in 24 patients, and 20 of these 24 (83.3%) lesions were diagnosed by bronchoscopy (Table 3). Positive diagnosis was made in 51 patients, negative diagnosis in 10 patients and incompletion diagnosis in 21 patients. Twenty-one of 31 patients who underwent a nondiagnostic rMSCT CT fluoroscopic guidance were confirmed to have lung cancer at surgery, and 1 patient was confirmed to have a benign at surgery. The location of the nodular lesions was 7 in the left upper, 37 in the right upper lobes, 1 in the lingual

lobe, 12 in the middle lobe, 9 in the left lower and 16 in the right lower lobe. The morphological data regarding their nodules were 25 solid nodules, 52 ground glass nodules with high density (mixed nodular pattern) and 5 pure ground glass nodules (non-solid nodular pattern) on chest CT scan. In all patients, re-adjustment using rMSCT fluoroscopy was required before biopsy, aspiration or brushing. Table 3 shows the diagnostic yield according to lesion size: <10 mm in diameter, 9 of 21 patients (42.9%); 11–15 mm, 13 of 24 patients (54.2%); 16–20 mm, 12 of 19 patients (57.9%); 21–25 mm; 8 of 9 patients (88.9%) and >25 mm in diameter, 9 of 9 patients (100%). The visualization and localization of the peripheral lesions under rMSCT fluoroscopy were good and each sampling method (brushing, aspiration and biopsy) was performed. In 21 of 82 patients, adequate bronchoscopy could not be performed because we could not accurately localize the correct bronchial subsegment associated with the lesion ($n = 14$) with MSCT fluoroscopy, or accurately slide the sampling instrument along the sides of the lesion or through the lesion ($n = 5$). In two patients, the ground-glass opacity could be detected under rMSCT. In 8 patients in whom the lesion could not be diagnosed and who had undergone rMSCT fluoroscopic guidance, the lesion resolved spontaneously, as demonstrated on follow-up CTs.[12] In 6 of 8 patients, the nodules or ground glass opacity disappeared on sequential CTs

Table 4   Diagnostic yield of bronchoscopy under rMSCT fluoroscopic guidance.

Lesion size (mm)	Peripheral lung lesions		
	rMSCT (diagnosed number/total number)	X-ray TV (diagnosed number/total number)	Significance
<10	9/21 (42.9%)	1/14 (7.7%)	$P = 0.028$
11–15	13/24 (54.2%)	2/12 (20%)	$P = 0.039$
16–20	12/19 (63.2%)	9/14 (64.3%)	NS
21–25	8/9 (88.9%)	9/12 (75%)	NS
>25	9/9 (100%)	20/26 (76.9%)	NS
All lesions	51/82 (62.2%)	41/78 (52.6%)	NS

Data are numbers and (percentages) of correctly diagnosed cases.
rMSCT: real-time multi-slice computed tomography; TV: television; NS: not significant.

Table 5   Radiation exposure.

Lesion size (mm)	Patients		Bronchoscopist
	Exposure time (s)		Radiation exposure (μSv)
< 10	330.3±170	925±476	93.5±67
10–15	343.7±203	962±567	65.1±47
16–20	387.3±144	1084±404	94.8±47
21–25	253.5±83.1	710±233	43.9±28
>25	210.4±138	589±386	75.1±45
Conventional CT	12	474	
Conventional with thin-section CT	22	869	

Data are mean±standard deviation.
CT: computed tomography.

after the administration of broad-spectrum anti-biotic therapy after rMSCT fluoroscopic guidance.

Comparison of X-ray TV and rMSCT CT fluoroscopic guidance for performing bronchoscopy

Seventy-eight patients were enrolled in the X-ray TV fluoroscopic guidance for performing the bronchoscopy arm of this study. At the Iiyama Red Cross Hospital, the diagnostic yield of X-ray TV fluoroscopic guidance in all lesions was 52.6% (41 of 78 patients). The proportions of cases with accurate final diagnoses by X-ray TV fluoroscopic guidance and rMSCT fluoroscopic guidance for performing bronchoscopy were not significantly different. The diagnostic yields of X-ray TV fluoroscopic guidance and rMSCT fluoroscopic guidance for lung lesions were: for lesions <10 mm in diameter, 7.7% and 43%; 11–15 mm, 20% and 54%; 16–20 mm, 64% and 63%; 21–25 mm, 75% and 89%; >26 mm in diameter, 77% and 100%, respectively. These results indicate that the diagnostic yield of

rMSCT fluoroscopic guidance for performing bronchoscopy was significantly superior to that of X-ray TV fluoroscopic guidance for lesions measuring < 15 mm ($P < 0.001$) (Table 4).

Radiation exposure

Patients and the bronchoscopist were exposed to a mean radiation dose of 912.2 μSv (range, 138–2313 μSv) and 75.2 μSv (range, 16–208 μSv), respectively. The mean time of the rMSCT fluoroscopic procedure was 325.8 s (range, 49.3–826 s). Table 5 shows the radiation dose and time of bronchoscopy according to lesion size.

Complications

No significant bleeding occurred during the procedures and no dyspnea or ventilatory compromise was noted. None of the procedures resulted in pneumothorax, pneumomediastinum or bacteremia.

Discussion

This study is the first to compare the diagnostic yields of X-ray TV fluoroscopic guidance and rMSCT fluoroscopic guidance for performing bronchoscopy, although it is a historical comparison between the two techniques. However, this study does not serve as a control study unless the nodules are truly matched in terms of their size and location density, although we assessed the diagnostic yield of rMSCT fluoroscopic guidance for peripheral nodules, and compared these results with those of X-ray TV fluoroscopic guidance conducted by a single physician (K.T.). However, the present data can show the use of rMSCT fluoroscopic guidance in patients with peripheral lung lesions. Compared with CT-guided percutaneous thoracic needle biopsy, bronchoscopy has low sensitivity and false negative results. CT-guided percutaneous thoracic needle biopsy may be considered as the first diagnostic step, especially for very small, peripheral and easily accessible lesions. We did not perform CT-guided biopsy for peripheral lesions, although the frequency of pleural dissemination was low. Surgical excision was also performed for the final diagnosis of lung cancer. However, some patients were anxious or refused surgery, or hoped a final diagnosis of the pulmonary lesion could be made before surgery. Moreover, some studies showed that CT-guided bronchoscopy for transbronchial needle aspiration is a safe and efficient tool for providing diagnostic material from mediastinal lymph nodes and peripheral nodules.[8,9,11] Therefore, we performed rMSCT fluoroscopic guidance for the diagnosis of pulmonary lesions and to compare its diagnostic accuracy with that of X-ray TV fluoroscopic guidance. However, the selected approach depends on the location and extent of lesions, as well as other considerations such as referral patterns, expertise and preferences, in addition to the availability of the necessary equipment.

In our study, diagnosis was confirmed by biopsy in 51 of 82 patients. This compares favorably with recent studies in which the overall rate of accurate diagnosis was 50–70% for lesions of various sizes.[7] The sensitivity was markedly better than that of fiberoptic bronchoscopy conducted by Baaklini et al.[7] who reported a positive bronchial wash in 71 of 177 cases (40%). Our conventional diagnostic procedures of bronchoscopy included needle aspiration, brush and transbronchial biopsy. Transbronchial biopsy is the only bronchoscopic method that allows obtaining a biopsy specimen, hence allowing diagnosis of benign lesions. Although transbronchial biopsy is associated with a higher risk of bleeding and pneumothorax than transbron-

chial needle aspiration,[12] we performed endobronchial biopsy as one of the bronchoscopic procedures when possible. Consequently, it is possible to provide a histological diagnosis by the transbronchial biopsy. Our results showed certain benefits of rMSCT fluoroscopic guidance for performing bronchoscopy. The diagnostic procedure enabled the detection of small lesions, which could not be detected by X-ray TV fluoroscopic guidance. It is important to accurately determine the location of lesions when planning the biopsy and needle aspiration, especially for small peripheral lesions and the lymph nodes adjacent to the major blood vessels. Transbronchial needle aspiration under the rMSCT fluoroscopic guidance can visualize the needle and select an optimal site for needle penetration and can confirm the depth and angle of the needle in real time during the procedure. Although no complications occurred in our study, we performed a CT sequence immediately upon completion of the procedure, which would have permitted immediate detection of and intervention for pneumothorax or hemorrhage.

The most important drawback of rMSCT fluoroscopic guidance for performing bronchoscopy is the radiation exposure of patients, bronchoscopist and assistants (Table 5). The potential concern related to this technique is the use of several minutes of fluoroscopy. Conventional X-ray TV fluoroscopic guidance dose parameters are approximately 90 kV and 4 mA per second. In comparison, these parameters are 120 kV and 150 mA per second in the conventional CT fluoroscopy but only 120 kV and 10 mA per second in our MSCT fluoroscopy. The dose used in MSCT fluoroscopy was at least double that used for conventional X-ray TV-guided fluoroscopy. In conventional CT, exposure of the entire lung requires movement of the sliding table in about 12 s, resulting in a maximum skin dose level of approximately 395 μSv. This time was as much as ~22 s, making the maximum skin dose level of ~869 μSv in conventional CT combined with thin-section CT. As shown in Table 5, this radiation exposure is almost the same as that of rMSCT fluoroscopic bronchoscopy (mean maximum skin dose level; 852 μSv, mean bronchoscope procedure time; 304 s). The bronchoscopist was exposed to a mean maximum radiation dose of 69.5 μSv. Unlike conventional fluoroscopy MSCT fluoroscopy employs a tightly collimated beam (2 mm) that confines to a narrow area. The radiation dose is further dissipated because the sliding table method used in this procedure limits exposure to any particular region. Moreover, we reconstructed the virtual bronchoscopy and selected the precise bronchus with the nodule before performing bronchoscopy.

McAdams et al.[13] reported the use of virtual bronchoscopy for guidance during the transbronchial biopsy procedures. Their results suggested that imaging guidance might improve the diagnostic sensitivity for malignant nodule. Although virtual bronchoscopy provides a "road map" that could be viewed by the bronchoscopist before performing bronchoscopy, it does not provide direct guidance during the procedure. The usefulness of virtual bronchoscopy is unfortunately limited because it cannot confirm the correct location of the peripheral bronchus, due to its limited success in reconstructing the peripheral bronchi in detail. However, we believe that virtual bronchoscopy is beneficial as it shortens the procedure of MSCT fluoroscopy since the virtual images could correctly detect fourth-order bronchi under 1-mm collimation high-resolution CT.

rMSCT-fluoroscopic guidance, as well as X-ray TV fluoroscopy are associated with other risk factors. The minute specimens obtained by the BF 3C40 procedure make it difficult to establish a definitive histopathological diagnosis, especially ground-glass opacity with Noguchi type A and type B or adenomatous atypical hyperplasia. Lesions detected by chest CT screening mostly appears as small-diameter lesions. A large proportion of small nodules do not invade the neighboring bronchus. Therefore, even with the brush instrument placed in the center of the lesions, it is difficult to obtain sufficient material from alveolar-lining tumors. Specimens obtained by bronchoscopy are only tiny parts compared with the specimens obtained by operations, and are unsuitable to assess the histological grade of the whole lesion apparent on MSCT. Moreover, it is often difficult to maneuver the biopsy instruments to reach the site of the peripheral lesion, due to the limited flexion inherent in such instruments, compared with brush instruments. In some cases, the peripheral nodules could not be accessed by biopsy forceps but could be reached by the brush instrument. In this study, it was difficult to make a definitive diagnosis for small nodules measuring < 10 mm without bronchial signs, using rMSCT fluoroscopic guidance. To obtain samples correctly from nodules < 10 mm in diameter, it is necessary to place the bronchoscope at a bronchus adjacent to the nodules, and to perform transbronchial biopsy. In four small nodules measuring < 10 mm, diagnosis could not be established using 3C40 bronchoscopy. Instead, we used ultrathin-bronchoscopy (Olympus BF XP 40, outer diameter: 2.8 mm, forceps channel: 1.2 mm) to improve the approach to the small nodules. That bronchoscopy allowed the approach of the deep part of the second-order bronchus better than 3C40

bronchoscopy, although no firm diagnosis could be made in any of these cases. For small nodules < 10 mm in diameter, rMSCT fluoroscopic guidance showed clearly superior accuracy compared with X-ray TV fluoroscopic guidance, although the diagnostic accuracy of the former procedure is not yet ideal.

The endoscopic ultrasound-guided bronchoscopy has been adapted for the central mass and peripheral nodules. Kikuchi or Kurimoto et al. reported that even when restricted to peripheral small nodules < 20 mm in diameter, the diagnostic sensitivity of endobronchial ultrasonography with guide sheath-guided transbronchial biopsy was 53% or 66%, respectively.[14,15] However, US cannot detect the nodules without solid component less than 15 mm in diameter although the data was not shown on our hospital. Therefore, the bronchoscopy under MSCT is more useful to reach a diagnosis than that under EBUS for the nodules without solid components less than 15 mm in diameter.

The final problem is the cost-utility of this technique. We calculated the cost of rMSCT fluoroscopic guidance for the performance bronchoscopy to be more expensive by $40 compared with X-ray TV fluoroscopic guidance. The screening cost for lung cancer by chest CT per person was $50, based on our 3-year CT screening program (Asakura et al., Japanese publication, 1999). Surgical excision was also performed for a final diagnosis of lung cancer. However, some patients may be anxious or refuse surgery, or hope a final diagnosis of the pulmonary nodule could be made before surgery. We commonly used to follow small nodules by performing serial CTs because its interval growth would be an indication for surgery. However, the cost of more than 2 follow-up CTs was more expensive than that of rMSCT fluoroscopic guidance. To establish a diagnosis at the time of first identification may could be more cost-effective compared with the cost of serial follow-up CTs.

Conclusions

Nodules of different sizes could be assessed using one or more diagnostic procedure. In bronchoscopic procedures for peripheral nodules, small nodules less than 10 mm should be diagnosed based on CT morphologic and density characteristics and the presence or absence of tumor growth tendencies as determined by serial follow-up CTs because of low diagnostic sensitivity of rMSCT fluoroscopic guidance for performing bronchoscopy. For lung

nodules of 10–15 mm in diameter and nodules of 16–20 mm not clearly visible on X-ray TV, rMSCT fluoroscopic guidance is a useful procedure based on the diagnostic sensitivity determined in our study. For nodules more than 20 mm in diameter, rMSCT- or X-ray fluoroscopic guidance for performing bronchoscopy could be selected.

Acknowledgments

References

1. Mountain CF. Revisions in the international system for staging lung cancer. *Chest* 1997;111:1710–7.
2. Sagawa M, Saito Y, Takahashi S, et al. Clinical and prognostic assessment of patients with resected small peripheral lung cancer lesions. *Cancer* 1990;66:2653–7.
3. Oda M, Watanabe Y, Shimizu J, et al. Extent of mediastinal node metastasis in clinical stage I non-small-cell lung cancer: the role of systematic nodal dissection. *Lung Cancer* 1998;22:23–30.
4. Wallace JM, Deutsch AL. Flexible fiberoptic bronchoscopy and percutaneous needle lung aspiration for evaluating the solitary pulmonary nodule. *Chest* 1982;81:665–70.
5. Fletcher EC, Levin DC. Flexible fiberoptic bronchoscopy and fluoroscopically guided transbronchial biopsy in the manage-
ment of solitary pulmonary nodules. *West J Med* 1982;136:477–83.
6. Chechani V. Bronchoscopic diagnosis of solitary pulmonary nodules and lung masses in the absence of endobronchial abnormality. *Chest* 1996;109:620–5.
7. Baaklini WA, Reinoso MA, Gorin AB, Sharafkaneh A, Manian P. Diagnostic yield of fiberoptic bronchoscopy in evaluating solitary pulmonary nodules. *Chest* 2000;117:1049–54.
8. Rong F, Cui B. CT scan directed transbronchial needle aspiration biopsy for mediastinal nodes. *Chest* 1998;114:36–9.
9. White CS, Templeton PA, Hasday JD. CT-associated transbronchial needle aspiration: usefulness of CT fluoroscopy. *Am J Roentgenol* 1997;169:393–4.
11. Goldberg SN, Raptopoulos V, Boiselle PM, Edinburgh KJ, Ernst A. Mediastinal lymphadenopathy: diagnostic yield of transbronchial mediastinal lymph node biopsy with CT fluoroscopic guidance—initial experience. *Radiology* 2000;216:764–7.
12. Libby DM, Henschke CI, Yankeievitz DF. The solitary pulmonary nodule: update 1995. *Am J Med* 1995;99:491–6.
13. McAdams HP, Goodman PC, Kussin P. Virtual bronchoscopy for detecting transbronchial needle aspiration of hilar and mediastinal lymph nodes: a pilot study. *Am J Roentgenol* 1998;170:1361–4.
14. Kikuchi E, Yamazaki K, Sukoh N, et al. Endobronchial ultrasonography with guide-sheath for peripheral pulmonary lesions. *Eur Respir J* 2004;24:533–7.
15. Kurimoto N, Miyazawa T, Okimasa S, et al. Endobronchial ultrasonography using a guide sheath increases the ability to diagnose peripheral pulmonary lesions endoscopically. *Chest* 2004;126:959–65.

Further reading

10. Hasegawa M, Sone S, Takashima S, et al. Growth rate of small lung cancers detected on mass CT screening. *Brit J Radiol* 2000;73:1252–9.

ORIGINAL ARTICLE

Measurement of Tumor Blood Flow Using Dynamic Contrast-enhanced Magnetic Resonance Imaging and Deconvolution Analysis: A Preliminary Study in Musculoskeletal Tumors

Yoshifumi Sugawara, MD,* Kenya Murase, PhD,† Keiichi Kikuchi, MD,* Kenshi Sakayama, MD,‡
Tatsuhiko Miyazaki, MD,§ Makoto Kajihara, MD,* Hitoshi Miki, MD,* and Teruhito Mochizuki, MD*

Objective: To measure tumor blood flow (TBF) using dynamic contrast-enhanced magnetic resonance imaging (DCE-MRI).
Methods: A DCE-MRI was performed using inversion recovery-preparation fast-field echo sequences. Dynamic data were obtained every 3.2 seconds for 2 minutes, immediately after gadolinium injection. In 14 patients with malignant musculoskeletal tumors, TBF maps were generated pixel-by-pixel by deconvolution analysis. For preclinical studies, muscle blood flow in 5 volunteers and signal intensities of different gadolinium concentrations were measured.
Results: There was a good linear relationship between signal intensities and gadolinium concentrations ($r = 0.989$, $P < 0.001$, at gadolinium concentrations ≤ 2 mmol/L). The average value of muscle blood flow in volunteers was 11.1 ± 2.7 mL·100 mL^{-1}·min^{-1}. In 14 patients with musculoskeletal tumors, TBF showed wide variances: the lowest of 9.6 mL·100 mL^{-1}·min^{-1} in liposarcoma and the highest of 182.0 mL·100 mL^{-1}·min^{-1} in osteosarcoma. After chemotherapy, the TBF values (7.9, 11.0, and 11.7 mL·100 mL^{-1}·min^{-1}) in the good responders were lower than those (26.8, 31.0, and 62.4 mL·100 mL^{-1}·min^{-1}) in the poor responders.
Conclusions: A functional map of TBF generated by DCE-MRI and deconvolution analysis would be a promising tool for evaluating tumor blood flow in vivo.

Key Words: musculoskeletal tumor, MRI, tumor blood flow, treatment response

(*J Comput Assist Tomogr* 2006;30:983–990)

I t has been reported that angiogenesis correlates with tumor growth, invasion, and metastasis.[1–4] In vivo tumor blood flow (TBF) increases as a result of angiogenesis, and it plays a key role in tumor growth and formation of metastasis.[5] Measurement of TBF in vivo may be valuable in the assessment of malignant tumors and their treatment responses. Because several antiangiogenic/antivascular agents are currently in clinical trials,[5,6] it is warranted to measure TBF noninvasively in vivo. However, in clinical practice, how to noninvasively measure TBF in vivo has not been established.

Tumor blood flow has been measured with Doppler ultrasonography or positron emission tomography (PET), although several limitations in clinical use have been reported.[7,8] Doppler ultrasonography has limited sensitivity for recognizing blood flow in deeply located tumors and limited reproducibility because of its dependence on the examiner's experience.[7] Quantitative measurement of TBF could be done by PET using diffusible tracers such as oxygen-15 water,[8,9] however, it requires a cyclotron nearby, and such accessibility is limited.

With recent advances in magnetic resonance (MR) systems and ultrafast magnetic resonance imaging (MRI) sequences, dynamic data with high spatial resolution can be obtained.[10–12] These advances have enabled the monitoring of dynamic changes in signal intensities in vivo after a bolus injection of contrast materials. However, reports concerning the measurement of TBF using dynamic contrast-enhanced MRI (DCE-MRI) are limited.[13] According to the indicator dilution theory[14] and the nonparametric deconvolution technique based on the singular value decomposition proposed by Ostergaard et al,[12] Pahernik et al[13] recently reported that, in experimental animal models, imaging of TBF could be obtained in vivo using DCE-MRI and deconvolution analysis. However, to the best of our knowledge, the feasibility of this technique has not been reported for measurement of TBF in humans. In this study, we developed methods for noninvasive measurement of TBF in human tumors using DCE-MRI and deconvolution analysis.

MATERIALS AND METHODS

Human Study

Subjects

Dynamic contrast-enhanced MRI was performed on 5 normal healthy volunteers (4 men and 1 woman; age range,

181

25–42 years; mean age, 32 years) and on 14 patients (7 men and 7 women; age range, 14–81 years; mean age, 47 years) with histologically proven malignant bone tumors (n = 5) and soft-tissue tumors (n = 9). A total of 28 TBF measurements were performed, including 15 postchemotherapy studies on 6 patients (TBF measurements were performed only after chemotherapy on 2 patients). The patients' data are summarized in Table 2. The study was conducted in accordance with the international standards of good clinical practice and the World Medical Association Declaration of Helsinki (Helsinki, Finland, 1964) and subsequent amendments (Tokyo, Japan, 1975; Venice, Italy, 1983; Hong Kong, 1989; and Somerset West, Republic of South Africa, 1996). Informed consent was obtained from each subject before enrollment in the study.

In 13 of 14 patients, surgical resections were performed, and pathological correlations were available. A patient with malignant lymphoma (patient 2) was only treated with chemotherapy; surgical resection was not performed. In 6 patients who received presurgical chemotherapy (patients 1, 8, 9, 10, 11, and 13), the response grading of the tumor was performed by 1 pathologist (T.M.), according to the previous report by Rosen et al.[15] In brief, the amount of tumor necrosis induced by chemotherapy was measured in the largest slice of the resected specimen and graded as follows: grade 1 = no or little effect of chemotherapy (tumor necrosis <50%); grade 2 = a partial response to chemotherapy (some histological sections demonstrated areas of viable tumor; tumor necrosis >50% but <90%); grade 3 = good response to chemotherapy, with only scattered foci of viable tumor cells (tumor necrosis >90%); and grade 4 = no viable-appearing tumor cells noted in any of the histological sections (tumor necrosis of 100%).

Dynamic Contrast-enhanced Magnetic Resonance Imaging

All MR studies were performed on a 1.5-T superconducting MR system (Gyroscan ACS-NT; Philips Medical Systems, Best, The Netherlands). For blood flow measurement, DCE-MRI was performed using inversion recovery-preparation fast-field echo sequence (repletion time [TR]/echo time [TE]/inversion time [TI] = 7.7/3.9/280 milliseconds, flip angle = 10 degrees, rectangular field of view = 380 × 190 mm, matrix = 256 × 128) with a slab thickness of 30 mm and 5 partitions (slice thickness = 6 mm). With the patient on the supine position, a 10- to 15-mL bolus injection of gadolinium chelate (0.5 mmol/mL) was injected into an antecubital vein followed by an injection of 20 mL of saline with an MR-compatible power injector. Dynamic data were obtained every 3.2 seconds for approximately 2 minutes (a total of 40 dynamic scans), immediately after the bolus injection. In the volunteers, DCE-MRI studies were performed at the level of the thigh. In the patients' studies, after conventional precontrast MR imaging with T1- and T2-weighted spin-echo sequences (T1: TR = 400 milliseconds, TE = 15 milliseconds; T2: TR = 2000 milliseconds, TE = 100 milliseconds), the largest slices of tumors were selected for the following DCE-MRI studies.

Data Analysis of Dynamic Contrast-enhanced Magnetic Resonance Imaging

All DCE-MRI data were transferred to a postprocessing workstation and analyzed using our proprietary software developed on MATLAB (The Mathworks Inc, Natick, Mass). The local changes in signal intensity during bolus passage were computed pixel-by-pixel. For a reduction of statistical noise, time smoothing was performed using an averaging filter with a weight of (0.25, 0.5, and 0.25). The arterial input function (AIF) [$C_a(t)$] was obtained by using fuzzy c-means clustering, which allowed automatic and accurate determination of arterial input.[16] According to the indicator dilution theory for intravascular contrast agents,[14] the time-dependent concentration curve of contrast agent in a volume of interest (VOI) [$C_{VOI}(t)$] is assumed to be expressed as:

$$C_{VOI}(t) = BF \int_0^t C_a(\tau) R(t-\tau) d\tau \qquad (1)$$

in which BF denotes blood flow, $C_a(t)$ represents the time-dependent AIF, and $R(t)$ represents the residue function. The residue function is the relative amount of contrast agent in the VOI in an idealized perfusion experiment, in which a unit area bolus was instantaneously injected [$R(0) = 1$] and subsequently washed out by perfusion [$R(\infty) = 0$]. It is known from Equation 1 that the initial height of the deconvolved time-concentration curve equals BF. In this study, we generated BF images by solving Equation 1 pixel-by-pixel using a nonparametric deconvolution technique based on singular value decomposition, as described in detail by Ostergaard et al.[12] The nonparametric deconvolution technique based on singular value decomposition allows estimation of flow relatively independent of the underlying vascular structure and volume even at the low signal-to-noise ratio associated with pixel-by-pixel deconvolution. In the volunteers, blood flow measurements in normal muscles at the level of the thigh were performed twice within a week. Arterial input function was obtained from the femoral artery, automatically using fuzzy c-means clustering,[16] and the mean blood flow of the femoral quadriceps muscle was measured. In the patients, AIF was obtained from the artery near the tumor, and a functional map of TBF was generated. On the functional TBF maps, the regions of interest were placed on the entire tumor and on the surrounding or contralateral normal tissues, referring to the conventional contrast-enhanced T1-weighted images; then, the mean TBF and the mean normal blood flow were obtained. In patients who received presurgical chemotherapy, the values of TBF before and after chemotherapy were compared.

Phantom Study

To validate the relationship between gadolinium concentration and MR signal intensity, 15 phantoms (each approximately 2 cm in diameter and 50 mL in volume) filled with distilled water and different amounts of gadolinium chelate were prepared. The gadolinium concentrations in each of the phantoms were as follows: 0, 0.2, 0.4, 0.6, 0.8, 1.0, 2.0, 3.0, 4.0, 5.0, 6.0, 7.0, 8.0, 9.0, and 10.0 mmol/L. The signal intensity of each phantom was measured using the
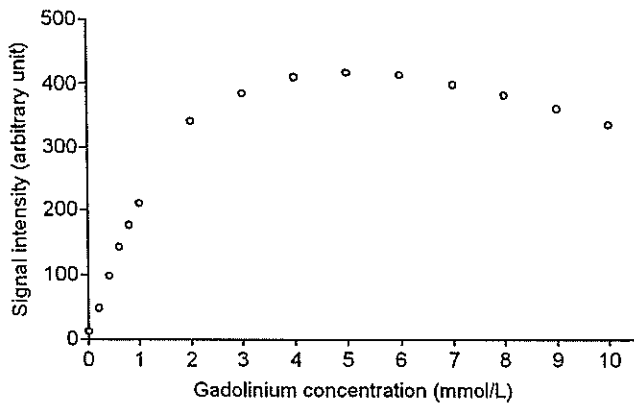
984

FIGURE 1. Relationship between gadolinium concentration (mmol/L) and signal intensity (arbitrary unit). In the lower range of gadolinium concentration, there is a good linear relationship between gadolinium concentrations and signal intensities ($r = 0.989$, $P < 0.001$, at gadolinium concentrations ≤ 2 mmol/L).

aforementioned 1.5-T MR system and inversion recovery-preparation fast-field echo sequence. The region of interest was placed in the center of each phantom, and the mean values of signal intensity (arbitrary units) were obtained. The relationship between signal intensity and gadolinium concentration was analyzed by the Spearman correlation coefficient and linear regression.

RESULTS

Phantom Study

The relationship between the gadolinium concentration and the measured signal intensity is shown in Figure 1. Within the lower range of gadolinium concentrations, there was a good linear relationship between the measured signal intensity and the gadolinium concentration ($r = 0.989$, $P < 0.001$, at gadolinium concentrations ≤ 2 mmol/L; Fig. 1). However, the signal intensity did not increase relative to the increase of gadolinium concentration at the higher range of gadolinium concentrations, and the signal intensity
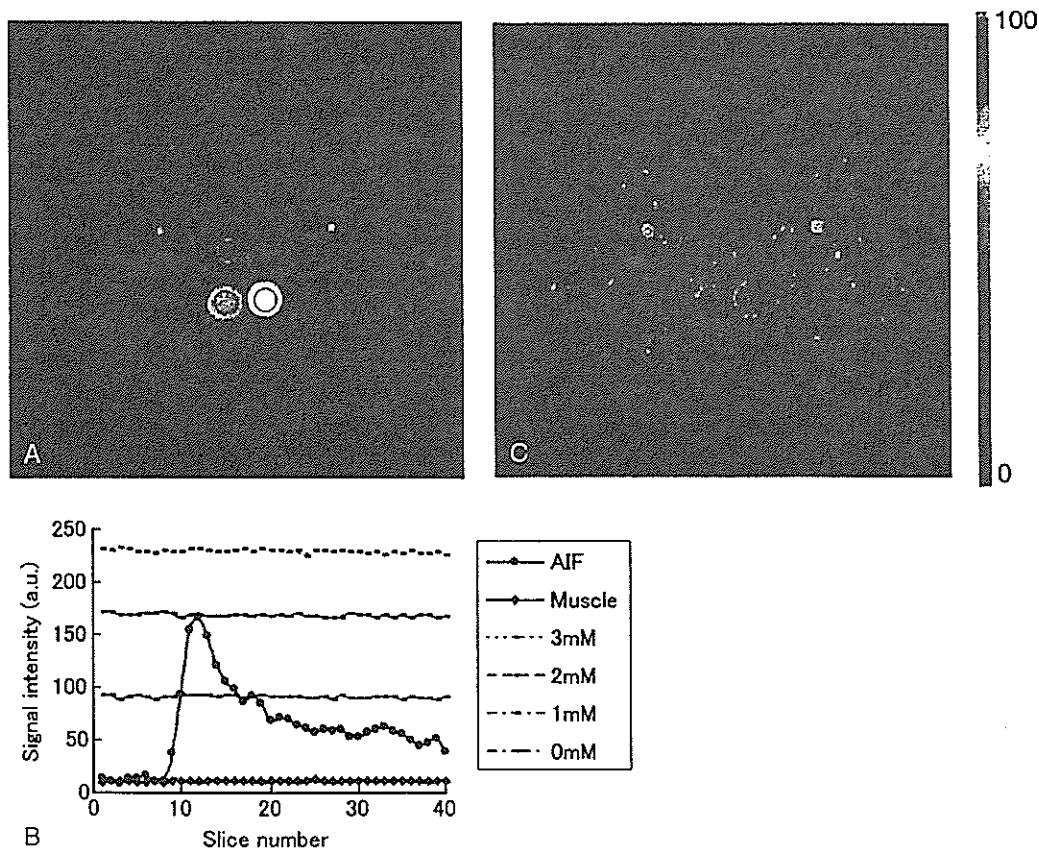

FIGURE 2. (A) An example of regions of interest and (B) signal intensity–time curves in the femoral artery, muscle, and phantoms of gadolinium concentrations of 0, 1, 2, and 3 mmol/L. The AIF was obtained from the signal intensity–time curve of the femoral artery immediately after a 10-mL bolus injection of gadolinium. The peak signal intensity of AIF was almost equal to the signal intensity of the phantom of gadolinium concentration of 2 mmol/L. (C) A functional map demonstrated the blood flow pixel-by-pixel with a color bar scale of 0 and 100 mL·100 mL^{-1}·min^{-1}.

     985

TABLE 1. Muscle Blood Flow in Healthy Volunteers

Volunteer No./ Age (y)/Sex	Blood Flow (mL·100 mL^{-1}·min^{-1})	
	First Measurement	Second Measurement
1/26/M	12.3 ± 4.3	12.2 ± 5.0
2/25/F	7.8 ± 3.6	7.2 ± 3.1
3/35/M	16.0 ± 6.0	12.0 ± 6.3
4/31/M	13.0 ± 5.1	11.6 ± 4.6
5/42/M	10.3 ± 5.0	8.6 ± 3.7

Data indicate mean ± SD.

decreased when the gadolinium concentration was greater than 5 mmol/L.

Blood Flow in Muscles of Volunteers

In all volunteers, a good AIF was obtained from the femoral artery. The signal intensity of the femoral artery was almost equal to that of the phantom with a gadolinium concentration of 2 mmol/L (Fig. 2). The mean blood flow in the femoral quadriceps muscles ranged from 7.8 ± 3.6 mL·100 mL^{-1}·min^{-1} to 16.0 ± 6.0 mL·100 mL^{-1}·min^{-1} (average,

11.9 ± 3.1 mL·100 mL^{-1}·min^{-1}) in the first measurement, and those in the second measurement ranged from 7.2 ± 3.1 mL·100 mL^{-1}·min^{-1} to 12.2 ± 5.0 mL·100 mL^{-1}·min^{-1} (average, 10.3 ± 2.3 mL·100 mL^{-1}·min^{-1}) (Table 1). The average value of normal muscle blood flow in 10 measurements of 5 healthy volunteers was 11.1 ± 2.7 mL·100 mL^{-1}·min^{-1}.

Tumor Blood Flow in Patients

In 14 patients with bone and soft-tissue tumors (5 bone tumors and 9 soft-tissue tumors), there were wide variances in TBF (Table 2); the lowest was 9.6 mL·100 mL^{-1}·min^{-1} in a liposarcoma (patient 3), and the highest was 182.0 mL·100 mL^{-1}·min^{-1} in an osteosarcoma (patient 11). The TBF values of 2 liposarcomas (TBF = 9.6 mL·100 mL^{-1}·min^{-1} and 24.1 mL·100 mL^{-1}·min^{-1}) and of 1 chondrosarcoma (TBF = 17.3 mL·100 mL^{-1}·min^{-1}) were lower than the TBF values of the other malignant tumors (TBF ranged from 36.4 mL·100 mL^{-1}·min^{-1} to 182.0 mL·100 mL^{-1}·min^{-1}).

In 6 patients who received presurgical chemotherapy (patients 1, 8, 9, 10, 11, and 13), substantial decreases in TBF were demonstrated after chemotherapy. The tumor responses

TABLE 2. Blood Flow in Patients With Bone and Soft-Tissue Tumors

Patient No./ Age (y)/Sex	Study No.	Diagnosis	BT/STT	Chemotherapy	Blood Flow (mL·100 mL^{-1}·min^{-1})	
					Tumor	Normal
1/43/M	1	Leiomyosarcoma	STT	Before	42.6	12.0
	2			After (1)	19.0	10.0
	3			After (2)	12.8	9.7
	4			After (3)	11.0	6.9
2/51/M	5	Lymphoma	STT	Before	70.0	9.7
3/79/M	6	Liposarcoma	STT	None	9.6	8.9
4/75/F	7	Leiomyosarcoma	BT	None	57.7	13.2
5/58/F	8	Liposarcoma	STT	None	24.1	13.8
6/64/M	9	MPNST	STT	None	77.1	13.9
7/31/F	10	Chondrosarcoma	BT	None	17.3	12.4
8/33/F	11	Ewing sarcoma	STT	Before	36.4	5.2
	12			After (2)	24.1	6.1
	13			After (3)	33.3	10.3
	14			After (5)	26.8	10.7
9/57/M	15	Osteosarcoma	STT	Before	63.3	6.5
	16			Before	79.5	12.1
	17			After (1)	49.3	11.5
	18			After (2)	29.7	12.0
	19			After (3)	31.0	10.6
10/14/F	20	Osteosarcoma	BT	After (2)	89.6	12.3
	21			After (5)	62.4	16.1
11/15/F	22	Osteosarcoma	BT	Before	182.0	7.5
	23			After (4)	23.4	2.8
	24			After (8)	17.9	6.6
	25			After (8)	7.9	3.0
12/47/M	26	Myxofibrosarcoma	STT	None	104.9	5.9
13/15/M	27	Osteosarcoma	BT	After (8)	11.7	10.9
14/81/F	28	MFH	STT	None	79.9	12.1

Numbers in parentheses represent the cycle numbers of chemotherapy.
BT indicates bone tumor; MFH, malignant fibrous histiocytoma; MPNST, malignant peripheral nerve sheath tumor; STT, soft-tissue tumor.
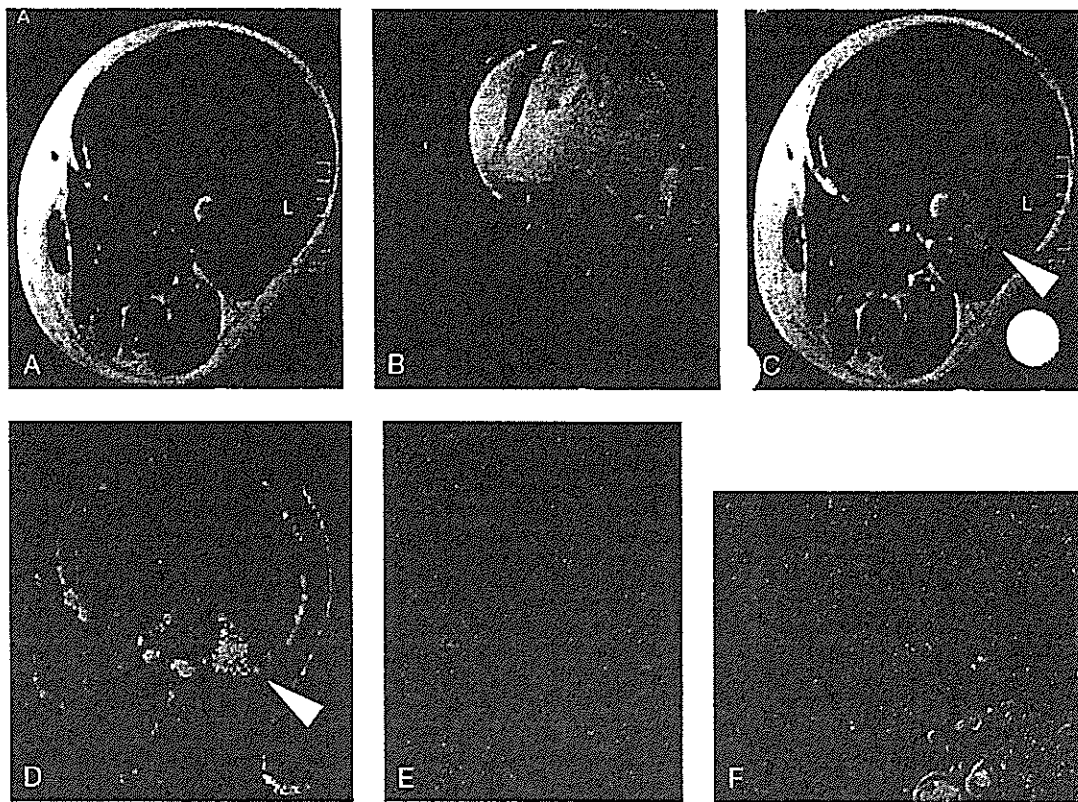
184

FIGURE 3. A 43-year-old man with leiomyosarcoma in the left thigh (patient 1). After 3 courses of chemotherapy, the tumor shows cystic change with hemorrhage, which presents (A) heterogeneous high intensity on a T1-weighted image and (B) very high intensity on a T2-weighted image. (C) Well-enhanced nodular lesion (arrowhead) is presented on the periphery of the tumor on contrast-enhanced T1-weighted image, which is clearly shown on (D) the TBF map. After surgical resection, the histopathologic sections show (E) a cystic lesion with hemorrhagic necrosis nearby a few layers of viable tumor cells and (F) a nodular lesion of viable tumor cells with marked neovascularization; a feeder artery is manifested (arrow) (hematoxylin-eosin stain, original magnification ×100).

to the presurgical chemotherapy were poor (tumor necrosis <90%) in 3 patients (grade 1 in patients 8 and 10 and grade 2 in patient 9) and good (tumor necrosis ≥90%) in 3 patients (grade 3 in patients 1 and 13 and grade 4 in patient 11). The TBF values after the last chemotherapy cycles in the good responders (11.0 mL·100 mL^{-1}·min^{-1} in patient 1, 7.9 mL· 100 mL^{-1}·min^{-1} in patient 11, and 11.7 mL·100 mL^{-1}·min^{-1} in patient 13) were lower than those in the poor responders (26.8 mL·100 mL^{-1}·min^{-1} in patient 8, 31.0 mL· 100 mL^{-1}·min^{-1} in patient 9, and 62.4 mL·100 mL^{-1}·min^{-1} in patient 10) (Figs. 3–6).

DISCUSSION

To apply DCE-MR images to tracer kinetic principles, a linear relationship between signal intensity and gadolinium concentration must be established. In the phantom study, there was a good linear relationship between the measured signal intensity and the gadolinium concentration in the lower range of gadolinium concentrations ($r = 0.988$, $P < 0.001$, at gadolinium concentrations ≤2 mmol/L; Fig. 1). The estimated

intra-arterial gadolinium concentration after a bolus injection can be considered to be within this range, as discussed below.

In clinical practice, it is difficult to directly measure the concentration of gadolinium in the artery after a bolus intravenous injection. Fritz-Hansen et al[17] previously measured in volunteers the arterial time-concentration curve from blood samples obtained from the brachial or radial artery. With correction for the catheter dispersion, the measured maximum concentration in the artery after a bolus intravenous injection of gadolinium (0.1 mmol/kg) was between 2.0 and 3.0 mmol/L.[17] They also reported that the gadolinium concentration measured by using inversion recovery turbo-FLASH (fast low-angle shot) in the descending aorta showed good agreement with the blood sampling data (with a variation of <7%). Given that the gadolinium concentration in the femoral artery is lower than in the descending aorta, we can estimate that the gadolinium concentration in the femoral artery was lower than that in the aorta (ie, 2.0–3.0 mmol/L). In this study, we confirmed that the peak of measured signal intensity of the femoral artery was within this range (gadolinium concentration between 2.0 and 3.0 mmol/L).
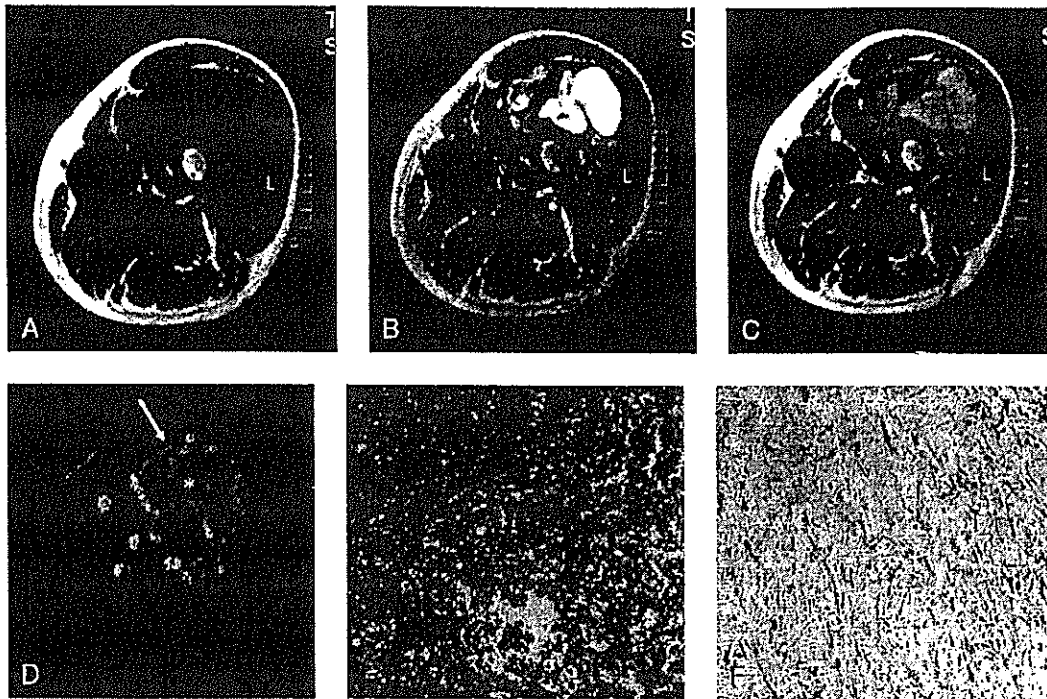
987

185

FIGURE 4. A 57-year-old man with extraskeletal osteosarcoma in the left thigh (patient 9). After 3 courses of chemotherapy, the tumor shows (A) low intensity on T1-weighted image, (B) mixed high intensity on T2-weighted image, and (C) inhomogeneous enhancement on contrast-enhanced T1-weighted image. (D) TBF map shows high blood flow in the periphery (arrow) with relatively low blood flow in the center (*), suggesting partial response. After wide resection, the histopathologic sections show (E) viable tumor cells with rich cellularity and vascularity in the periphery and (F) myxoid lesions of sparse vascularity in the center (hematoxylin-eosin stain, original magnification ×100). The response to the chemotherapy was considered as grade 2.

Accurate determination of AIF is necessary for quantification of blood flow using DCE-MRI and deconvolution analysis. Underestimation of AIF results in the overestimation of measured blood flow in tissues. This is of importance when a relatively small artery (ie, compared with the descending aorta used in the study by Fritz-Hansen et al[17]) is used for obtaining AIF. In the current study, fuzzy c-means clustering method was used in determining the accurate AIF while minimizing the above underestimation.[16] The details of this method were described in previous articles.[16,18] In brief, we chose the pixels showing the earliest and largest decreases in signal intensity after a bolus injection of gadolinium among the clustered data. This method has been recently applied to the quantitative assessment of pulmonary perfusion.[19]

In the current study, the mean value of normal muscle blood flow was 11.1 ± 2.7 mL·100 mL^{-1}·min^{-1} (average of a total of 10 measurements in 5 volunteers). This value was equivalent to the previous results (9.37 ± 4.88 mL·100 mL^{-1}·min^{-1}) in experimental animal studies using dynamic computed tomography and deconvolution analysis.[20] On the other hand, it has been reported that the muscle blood flow measured by PET using diffusible tracers such as oxygen-15 water was 3.12 ± 1.55 mL·100 mL^{-1}·min^{-1} in humans.[8,9] It has also been reported that the blood flow in noncontracting skeletal muscle of animals under anesthesia ranged from 5 to 10 mL·100 mL^{-1}·min^{-1}.[20,21] Thus, our methods may overestimate the normal muscle blood flow, whereas the PET

measurement may also underestimate the blood flow because of the partial volume effect caused by the lesser spatial resolution. Indeed, it has also been reported that the same muscle has much higher blood flow in conscious than in anesthetized animals. Moreover, these differences could be due in part to the differences of measuring methods, that is, the deconvolution-based methods with nondiffusible intravascular tracers versus the Fick principle-based methods with diffusible tracers.[8,12,13,20] The differences could also be attributed to the intrinsic differences in muscle blood flow measured in the studies; indeed, wide variances in blood flow were reported among muscle types and species.[21] Although not available in the current study, the validation studies between the in vivo DCE-MRI measurement and the other in vivo and ex vivo measurements (such as PET and autoradiography methods) in the same subjects would be recommended to elucidate these issues in the future.

In this preliminary study, we measured TBF in patients with musculoskeletal tumors in the leg because the AIF can be obtained constantly without motion artifacts. Dynamic data acquisition was stopped before 2 minutes, in only 1 patient (patient 11, study 22 in Table 2) because of the patient's motion, which created an artifact. We believe that our methods of TBF measurements using DCE-MRI can be applied to head and neck tumors and tumors in the pelvic cavity. Although it is still challenging to obtain AIF accurately in the torso, mainly because of motion artifacts,
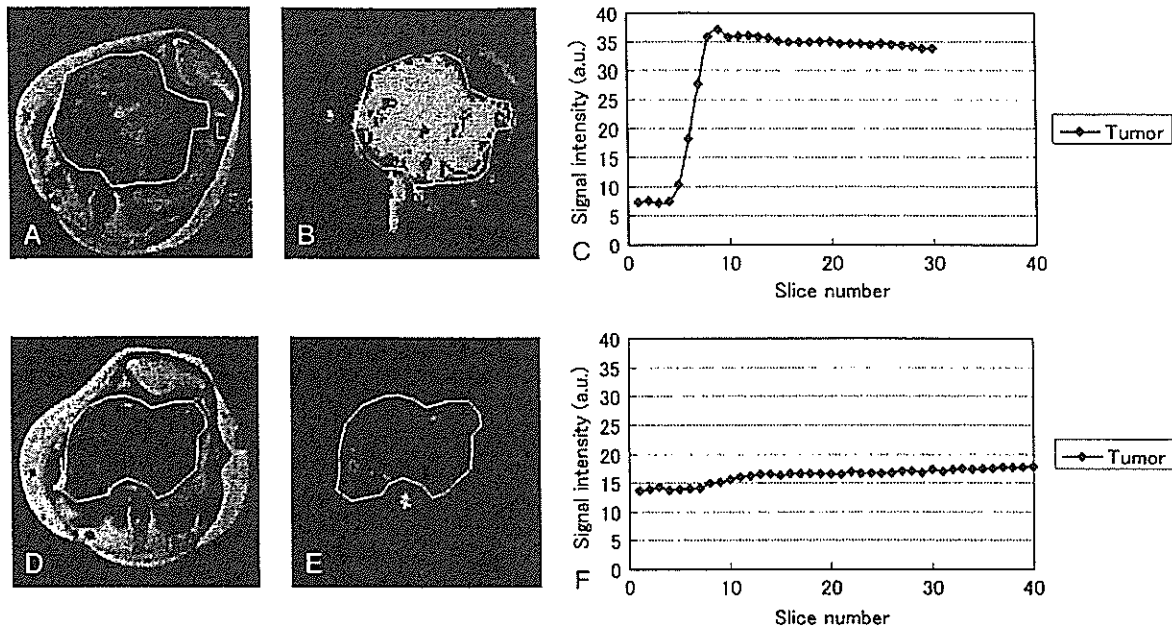
988

FIGURE 5. A 15-year-old girl with osteosarcoma in the left distal femur (patient 11). Before chemotherapy, (A) contrast-enhanced T1-weighted image, (B) TBF map, and (C) signal intensity–time curve of the tumor. After 8 cycles of chemotherapy, (D) contrast-enhanced T1-weighted image, (E) TBF map, and (F) signal intensity–time curve of the tumor. (A, D), After 8 cycles of chemotherapy, the tumor size decreased, but the enhanced area remained on the contrast-enhanced T1-weighted images. (C) Dynamic contrast-enhanced MR image before chemotherapy shows rapid increase of the signal intensity in the tumor followed by gradual decrease. Note that the dynamic study was stopped at the 30th slice because of the patient's motion. After chemotherapy, (F) the signal intensity increases gradually, and (E) the TBF map reveals remarkable decrease of TBF; (B) the TBF values are 182.0 mL·100 mL^{-1}·min^{-1} before chemotherapy and (E) 7.9 mL·100 mL^{-1}·min^{-1} after chemotherapy. At surgery, no viable tumor cells are observed in any of the histological sections, and the response to the chemotherapy was considered as grade 4.

it may be possible to apply this technique to tumors in other fields, if advances in MRI techniques can reduce the aforementioned limitations.
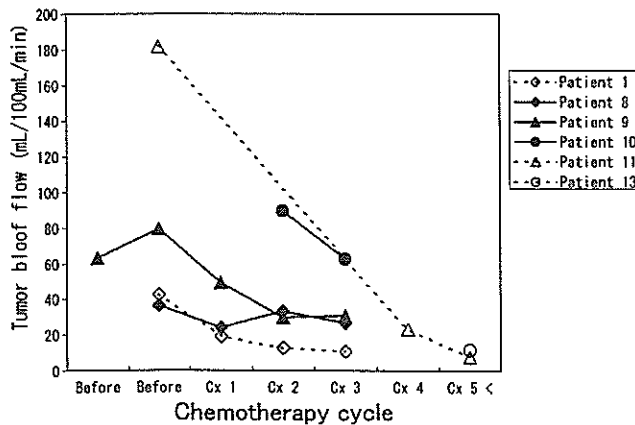

FIGURE 6. Changes of TBF in 6 patients who received presurgical chemotherapy (patients 1, 8, 9, 10, 11, and 13). In patient 9, a follow-up TBF measurement (3 weeks after the initial study) was repeated before chemotherapy. In patients 10 and 13, TBF measurements were performed only after chemotherapy. Substantial decreases of TBF are demonstrated after treatment, especially in the good responders (patients 1, 11, and 13).

As for musculoskeletal tumors, static contrast-enhanced T1-weighted images can differentiate necrosis from tumor but cannot clearly differentiate tumor from a chemotherapy-induced change. There have been several reports concerning DCE-MRI for evaluating tumor vascularization.[22-24] Verstraete et al[22] reported that there was a significant difference in the first-pass slope values between benign and malignant musculoskeletal lesions (36.2% per second vs 67.4% per second, $P < 0.001$). They also reported that the first-pass images depicted tissue vascularization rather than the presence or absence of malignancy, because there was an overlap in the slope values.[22] Dynamic contrast-enhanced MRI has also been shown to assist in detecting viable tumors in osteogenic sarcomas being treated with chemotherapy.[22-26] Dyke et al[25] recently reported that the histogram analysis of the initial slopes from tumors correlated well with the percentages of tumor necrosis. However, these measurements analyzed the changes of enhancement only in the tumors and did not consider the AIF; hence, quantitative evaluation of TBF has not been established. The changes in tumor enhancement could be affected by the change of AIF, which could be altered after treatment.

Although a relatively small number of patients were evaluated in this study, measurement of TBF seems to be promising in the objective evaluation of presurgical chemotherapeutic response. The functional map of TBF demonstrated substantial TBF decrease in the good responders

989